ISSN 1990-4789, Journal of Applied and Industrial Mathematics, 2019, Vol. 13, No. 1, pp. 93–102. © Pleiades Publishing, Ltd., 2019.
Russian Text © A.V. Marinenko, M.I. Epov, V.V. Olenchenko, 2019, published in Sibirskii Zhurnal Industrial'noi Matematiki, 2019, Vol. XXII, No. 1, pp. 63–73.

Solving Direct Problems of Electrical Resistivity Tomography for Media with High-Conductivity Irregular-Shaped Heterogeneities by an Example of a Multiple Well Platform

A. V. Marinenko[1*], M. I. Epov[1,2], and V. V. Olenchenko[1***]**

[1] *Trofimuk Institute of Petroleum Geology and Geophysics, pr. Akad. Koptyuga 3, Novosibirsk, 630090 Russia*

[2] *Novosibirsk State University, ul. Pirogova 2, Novosibirsk, 630090 Russia*

Received October 1, 2018; in final form, October 25, 2018; accepted December 15, 2018

Abstract—Under consideration is a multiple well platform where the metal pipes of various diameters that are located above and below ground act as interferences together with boreholes with metal tubing. The sought-for objects of study are the thawing zones located near the boreholes. Numerical calculations of direct problems are performed by the nodal finite element method implemented in the author's software package for solving the problems of electrical resistivity tomography.

DOI: 10.1134/S1990478919010113

Keywords: *direct problems, electrical resistivity tomography, finite element method, anomalies*

INTRODUCTION

In the geophysical research based on the direct current electrical resistivity tomography some preliminary numerical simulation is often necessary. This is especially topical in the case, when there is some information about the rocks for which tomography is performed. For example, such information is available on the geophysical sites where borehole drilling is carried out. The existing software for electrical resistivity tomography allows us to perform direct modeling only in the simplest cases and, first of all, to solve the problem of determining the number of electrodes and separation between them on site for successful detection of an object lying at certain depth.

The purpose of this study is to create an approach that allows us to investigate the effect on the resulting apparent resistance picture of the objects situated in the subsurface layer of earth and above it as well as to develop a strategy of minimizing this effect. A similar problem arises in the case of the same boreholes with metal tubing whose presence makes it very difficult to solve the inversion problem [1].

1. MODEL OF THE MEDIUM AND CHOICE OF THE WORKING INSTALLATION

As an example, consider the application of electrical resistivity tomography for multiple well platforms with the production gas wells [1]. The purpose of the tomography is to identify a possible low-resistance zone of permafrost thawing around the main borehole. At the site, the aboveground and underground metal structures are present in large quantities (pipes, piles, and casing). A model of a typical site, the basic metal structures, and the position of possible relatively low-resistance thawing zones is shown in Fig. 1. In the plot (a) the following notation is used: *1* denotes the metal supports hammered into the ground, *2* marks a metal pipe placed on the supports, *3* are the thawing zones near boreholes, *4* shows the metal-cased boreholes, and *5* is the area of electro-tomographic research.

First, the type of probe installation is chosen when planning works on electrotomography,. The most common is the Wenner-alpha installation [2] consisting of the four equidistant electrodes: Two feeding electrodes are located at the points A and B; and two measuring, at M and N (Fig. 2).

*E-mail: arkadiy@reqip.net
**E-mail: EpovMI@ipgg.sbras.ru
***E-mail: OlenchenkoVV@ipgg.sbras.ru

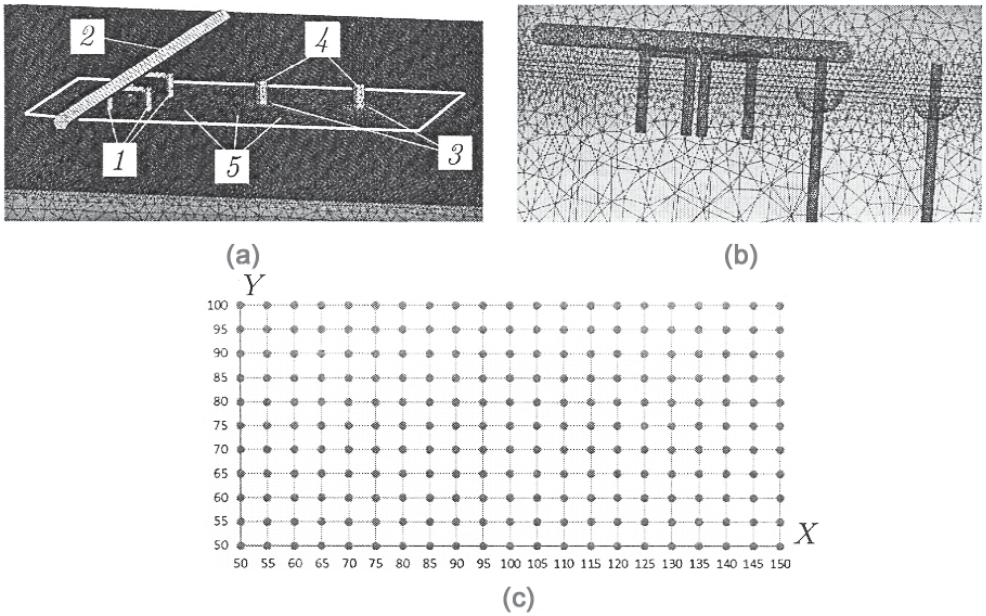

Fig. 1. Model of a typical site and areal system of excitation and measurement: (a) model of a multiple well platform with two boreholes, (b) example of tetrahedral partitioning of the simulation domain in the region of metal structures, and (c) uniform areal system of excitation and measurement.

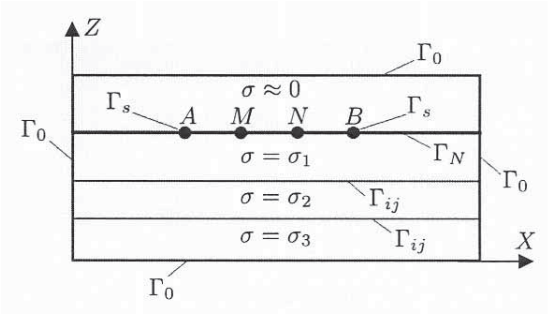

Fig. 2. The XOZ section of the layered computational domain under simulation.

2. MATHEMATICAL MODEL

On the feeding electrodes located at the points A and B of the Wenner-alpha installation, either some constant potential difference, or the value of the flowing down surface current is set. Mathematical statements for these two cases somewhat differ from one another. To begin with, we consider the first type of excitation.

Let us determine the electric field intensity in the medium for a given constant potential difference on the feeding electrodes. We assume that the upper half-space is occupied by the air with electrical conductivity close to zero. The conductive lower half-space without lateral inhomogeneities will be considered three-layered. We introduce a right-hand Cartesian coordinate system. The equation of the plane $Z = 0$ represents the daylight surface, and let the Z axis be upward-directed. Each of the layers is characterized by the values of electrical conductivity σ, magnetic μ and dielectric ε permeability. We will look for the values of the electric field at all points of the layered simulation domain (see Fig. 2).

Write the Maxwell system of equations in stationary mode [3]:

$$\text{rot } \vec{E} = 0, \tag{1}$$

$$\text{rot } \vec{H} = \sigma\vec{E} + \vec{J}, \tag{2}$$

$$\text{div } \vec{B} = 0, \tag{3}$$

$$\text{div } \vec{D} = 0. \tag{4}$$

Here, $\vec{E}$ is the electric field intensity (V/m), $\vec{D}$ is the electric induction (Kl/m^3), $\vec{H}$ is the magnetic field strength (A/m), $\vec{B}$ is the magnetic induction (Tl), σ is the specific electrical conductivity (Cm/m), and $\vec{J}$ is the density of extraneous surface current (A/m^2).

Consider the equations of state

$$\vec{D} = \varepsilon\vec{E}, \qquad \vec{B} = \mu\vec{H}.$$

Let a scalar electric potential φ be placed at B. It follows from (1) that

$$\vec{E} = -\text{ grad } \varphi. \tag{5}$$

Let Ω denote the domain in which the boundary value problem is considered. It consists of subdomains Ω_i with different electrical properties. On the boundary $\partial\Omega = \Gamma_0$ of the computational domain (see Fig. 2), the sought values are close to zero. If the medium above the ground-air boundary Γ_N does not contain conductive objects then the upper boundary $\partial\Omega$ of the computational domain is the union of Γ_N and Γ_S. On Γ_N the impermeability conditions are set for the normal component of current density:

$$\vec{n}\cdot\vec{J}|_{\Gamma_N} = \vec{n}\cdot\sigma\vec{E}|_{\Gamma_N} = \sigma\frac{\partial\varphi}{\partial n}\bigg|_{\Gamma_N} = 0,$$

where $\vec{n}$ is the unit outer normal to Γ_N.

On the electrode-medium boundary Γ_S the value of the potential $\varphi|_{\Gamma_S} = \varphi_0$ is given.

The function φ_0 on the segments of Γ_S that correspond to the location of the feeding electrodes is equal to the specified potential difference. For example, with the potential difference of 2 V the function φ_0 can be given as

$$\varphi_0 = \begin{cases} 1\,V, & \text{on } \Gamma_S \text{ at } A, \\ -1\,V, & \text{on } \Gamma_S \text{ at } B. \end{cases} \tag{6}$$

On the boundaries Γ_{ij} that distinguish subdomains with different specific electrical conductivity, the matching conditions for the electric field $\vec{E}$ are put as

$$[\vec{n}\times\vec{E}]_{\Gamma_{ij}} = 0, \qquad [\vec{n}\cdot\sigma\vec{E}]_{\Gamma_{ij}} = 0.$$

These conditions lead to the continuity of the potential φ and its normal derivative on the boundaries Γ_{ij}:

$$[\varphi]_{\Gamma_{ij}} = 0, \qquad \left[\sigma\frac{\partial\varphi}{\partial n}\right]_{\Gamma_{ij}} = 0,$$

where $\vec{n}$ is the unit outer normal to Γ_{ij}.

Thus, we arrive at the following boundary value problem:

$$-\text{div } \sigma\,\text{grad } \varphi = 0 \quad \text{in } \ \Omega = \bigcup_i \Omega_i, \tag{7}$$

$$\varphi|_{\Gamma_S} = \varphi_0, \tag{8}$$

$$\varphi|_{\Gamma_0} = 0, \tag{9}$$

$$\frac{\partial\varphi}{\partial n}\bigg|_{\Gamma_N} = 0 \tag{10}$$

(under absence of objects above the ground-air boundary);

$$[\varphi]_{\Gamma_{ij}} = 0, \tag{11}$$

$$\left[\sigma\frac{\partial\varphi}{\partial n}\right]_{\Gamma_{ij}} = 0. \tag{12}$$

Let us proceed to the second problem:

Given flowing down current on the feeding electrodes, determine the electric field in the medium.

This problem differs from the previous one in that, on the electrode-medium interface Γ_S, there is set the density value of the surface current flowing down from the feeding electrodes:

$$\vec{n}\cdot\vec{J}|_{\Gamma_S} = \vec{n}\cdot\sigma\vec{E}|_{\Gamma_S} = \sigma\frac{\partial\varphi}{\partial n}\bigg|_{\Gamma_S} = j_S,$$

where $\vec{n}$ is the unit outer normal to Γ_S.

The corresponding boundary value problem takes the form:

$$-\operatorname{div}\sigma\operatorname{grad}\varphi = 0 \quad \text{in} \quad \Omega = \bigcup_i \Omega_i; \tag{13}$$

$$\sigma\frac{\partial\varphi}{\partial n}\bigg|_{\Gamma_S} = j_S, \tag{14}$$

$$\varphi|_{\Gamma_0} = 0, \tag{15}$$

$$\frac{\partial\varphi}{\partial n}\bigg|_{\Gamma_N} = 0 \tag{16}$$

(under absence of objects above the ground-air boundary);

$$[\varphi]_{\Gamma_{ij}} = 0, \tag{17}$$

$$\left[\sigma\frac{\partial\varphi}{\partial n}\right]_{\Gamma_{ij}} = 0. \tag{18}$$

Let us obtain the variational formulations of these boundary value problems. We introduce the following spaces:

$$H^1 = \{\varphi\in L^2(\Omega)\mid \operatorname{grad}\varphi\in L^2(\Omega)\}, \qquad H_0^1 = \{\varphi\in H^1(\Omega)\mid \varphi|_{\partial\Omega} = 0\},$$

$$(u,v) = \int\limits_\Omega uv\,d\Omega + \int\limits_\Omega \operatorname{grad} u\cdot\operatorname{grad} v\,d\Omega,$$

$$\|u\|_{H^1}^2 = \int\limits_\Omega u^2\,d\Omega + \int\limits_\Omega (\operatorname{grad} u)^2\,d\Omega.$$

For the first of them, the variational formulation in the form of Galerkin has the form:

Find $\varphi\in H^1(\Omega)$ *such that* $\varphi-\varphi_0\in H_0^1(\Omega)$ *and for all* $v\in H_0^1(\Omega)$ *we have*

$$-\int\limits_\Omega \sigma\operatorname{grad}\varphi\cdot\operatorname{grad} v\,d\Omega + \int\limits_{\Gamma_0}\sigma\frac{\partial\varphi}{\partial n_0}v\,d\Gamma + \int\limits_{\Gamma_N}\sigma\frac{\partial\varphi}{\partial n}v\,d\Gamma + \int\limits_{\Gamma_{ij}}\sigma\frac{\partial\varphi}{\partial n_i}v\,d\Gamma + \int\limits_{\Gamma_{ji}}\sigma\frac{\partial\varphi}{\partial n_j}v\,d\Gamma = 0, \tag{19}$$

where $\Gamma = \Gamma_0\bigcup\Gamma_s\bigcup\Gamma_N\bigcup\Gamma_{ij}$, $\vec{n}_0$ *is the unit outer normal to* Γ_0, $\vec{n}_i$ *is the unit outer normal to* Γ_{ij}, $\vec{n}_j$ *is the unit outer normal to* Γ_{ji}, *and* $\vec{n}_i = -\vec{n}_j$.

In view of (9)–(12), equation (19) assumes the form

$$-\int\limits_\Omega \sigma\operatorname{grad}\varphi\cdot\operatorname{grad} v\,d\Omega = 0. \tag{20}$$

For the second problem, the variational formulation in the form of Galerkin is as follows:

Find $\varphi \in H_0^1(\Omega)$ *such that for every* $v \in H_0^1(\Omega)$ *we have*

$$-\int\limits_{\Omega} \sigma \operatorname{grad} \varphi \cdot \operatorname{grad} v \, d\Omega + \int\limits_{\Gamma_0} \sigma \frac{\partial \varphi}{\partial n_0} v \, d\Gamma + \int\limits_{\Gamma_S} \sigma \frac{\partial \varphi}{\partial n} v \, d\Gamma + \int\limits_{\Gamma_N} \sigma \frac{\partial \varphi}{\partial n} v \, d\Gamma + \int\limits_{\Gamma_{ij}} \sigma \frac{\partial \varphi}{\partial n_i} v \, d\Gamma + \int\limits_{\Gamma_{ji}} \sigma \frac{\partial \varphi}{\partial n_j} v \, d\Gamma = 0. \quad (21)$$

In view of (14)–(18), equation (21) assumes the form

$$-\int\limits_{\Omega} \sigma \operatorname{grad} \varphi \cdot \operatorname{grad} v \, d\Omega + \int\limits_{\Gamma_S} j_S v \, d\Gamma = 0. \quad (22)$$

The problems can be solved using the nodal finite element method by constructing some finite element analog of the variational equations (20) and (22). The computational domain and objects in it are divided into finite elements of certain type. On them, the basis functions are set [4]. In the present study, the linear basis functions on an irregular tetrahedral partition are used; i.e., on an individual finite element, the function is defined only at the vertices of the tetrahedron [5]. An example of such a partitionis shown in Fig. 1, b. The grid is condensed in the domains, where the objects affecting the simulation are situated and where the greatest spatial changes in the electric field are observed. Using the selected basis, we obtain a system of linear algebraic equations (SLAEs). To solve it, we use the conjugate gradient method [6] in a parallel implementation for graphics processors (GPU). Its solutions are the values of the potential φ at all grid nodes. The values of the vector electric field $\vec{E}$ are calculated according to (5).

3. NUMERICAL EXPERIMENT

Electrical resistivity tomography is often performed using a uniform areal system of excitation and measurement (see Fig. 1, c). Consider the profile in the immediate vicinity of the boreholes and metal supports partially immersed in the ground. Let us numerically solve the direct problem for one of the positions of the Wenner-alpha installation.

To conduct the electro-tomographic studies, we divide the domain (see Fig. 1, a) into cells as shown in Fig. 1, c. This approach makes it possible not to rebuild the finite-element grid at each position of the installation. It is also expedient to describe the position of the objects relative to the electrodes. The metal supports with diameter of 2 m are located at the centers of the following cells: (65–70 m, 60–65 m), (75–80 m, 60–65 m), (65–70 m, 80–85 m), and (75–80 m, 80–85 m). They are buried on 10 m and protrude above the daylight surface to height of 6 m. The diameter of the pipe lying on the supports is 4 m, its length is limited by the simulation domain. Casing pipes with diameter of 3 m are located at the centers of the following cells: (100–105 m, 75–80 m) and (125–130 m, 75–80 m). They are buried on 50 m and protrude above the daylight surface to height of 6 m. The presumed thawing zones are horizontal hemispheres with radius of 4.5 m.

The feeding electrodes with the unit current are situated at the points (60 m, 80 m) and (120 m, 80 m) immediately below the daylight surface $Z = 0$. The electric conductivity of the rocks is taken equal to 0.001 Cm/m, of the metal, $769 \cdot 10^4$ Cm/m, of the thawing zones, 0.01 Cm/m, and of air, 10^{-12} Cm/m. The simulation results for the distribution of electric potential and field along the profile $Y = 80$ m are presented in Fig. 3, where the following notation is used: *1* is a pipe, *2* is the right borehole, *3* is the left borehole, *4* is a part of the Π-shaped support.

On the map of electrical potential, the pipe lying on supports and the right borehole are marked (Fig. 3, a). On the map of the X-component of the electric field, both boreholes are marked (Fig. 3, b). The map of the Y-components (Fig. 3, c) gives the most complete picture of the metal structures; there we can see a part of the Π-shaped support and both boreholes. On the map of the vertical component of the electric field (Fig. 3, d), the buried objects are practically invisible.

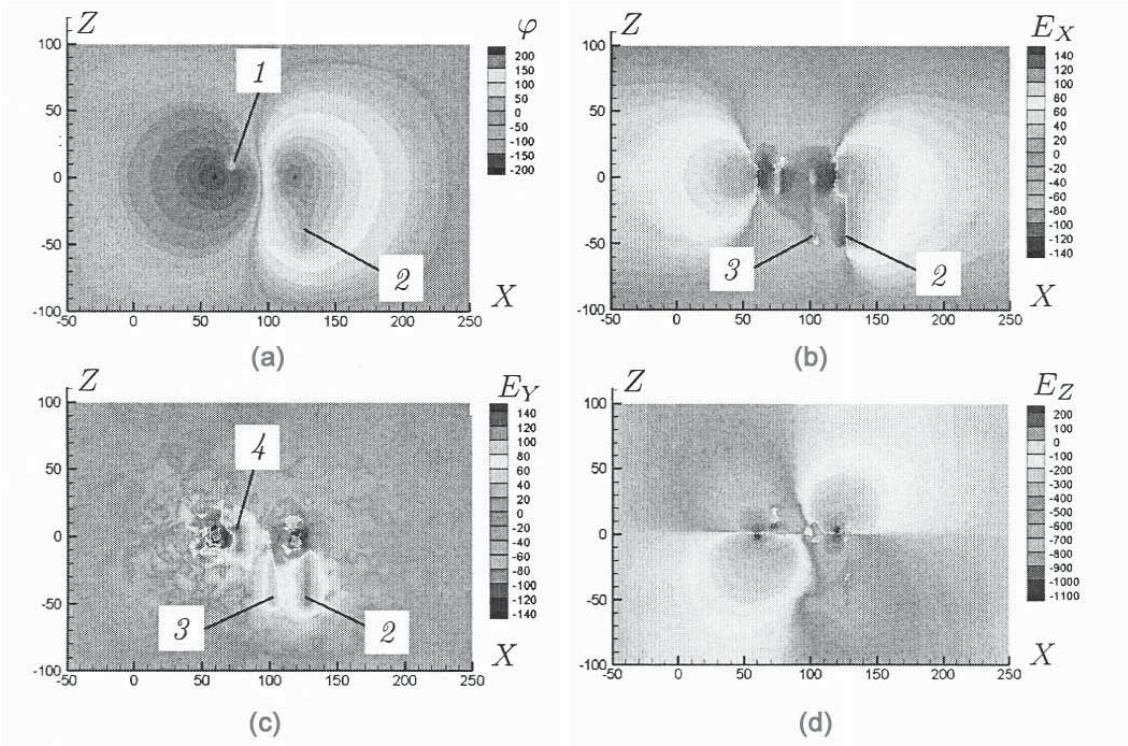

Fig. 3. The distribution of electrical potential and field in the XOZ section ($Y = 80$): the electric potential (a), the X-component (b), the Y-component (c), and the Z-component (d) of the electric field.

However, we note that, in real research, the measurements are performed only on the daylight surface (Fig. 1, c). In Fig. 4, the distribution is shown of the electric field components in the XOY section. Here the following notation is used: *1* denotes metal supports; *2* marks the left borehole and *3*, the right borehole; *4* is the left and *5* is the right thawing zone. In Fig. 4,a and b, the distribution is shown of horizontal components of the electric field for $Z = 0$.

The question remains important concerning the conditions for detecting the thawing zones. In Fig. 4 (plots c and d), the distribution is presented of the horizontal components of the electric field on the medium surface in the case when the thawing zones are absent. Fig. 4, e and f, show the map of anomalous values of the horizontal components of the electric field caused by the thawing zones.

Thus, changing the position of the feeding and receiving electrodes, we have the ability to restore, with certain degree of reliability, the true location of objects inside the medium under simulation.

At the first step, all measured signals are transformed into the apparent resistances (AR) [7, 8] $\rho_k = kU_{MN}/I_{AB}$, where U_{MN} is the measured potential difference between the electrodes M and N,

$$k = 2\pi \Big/ \left(\frac{1}{r_{AM}} - \frac{1}{r_{BM}} - \frac{1}{r_{AN}} + \frac{1}{r_{BN}} \right)$$

stands for the installation coefficient, and I_{AB} is the current in the line AB.

To construct a continuous distribution of AR, we interpolated the values using either the Delaunay algorithm [9] or the Voronoi diagrams [10].

A separate question consists in some realistic estimates for the propagation distance. According to [2], they are determined by the following main factors: the installation, the model, and the measurement errors. Traditionally, the propagation distance is associated with the distance between the feeding electrodes located at the points A and B, which we denote by AB and call the *installation spacing* that, in the case of the Wenner-alpha installation, coincides with the length of the segment AB, i.e., the distance between the feeding electrodes. The earliest of the mentioned estimates that equals $AB/2$ was obtained for the four-electrode Schlumberger installation [11]. Then it was refined

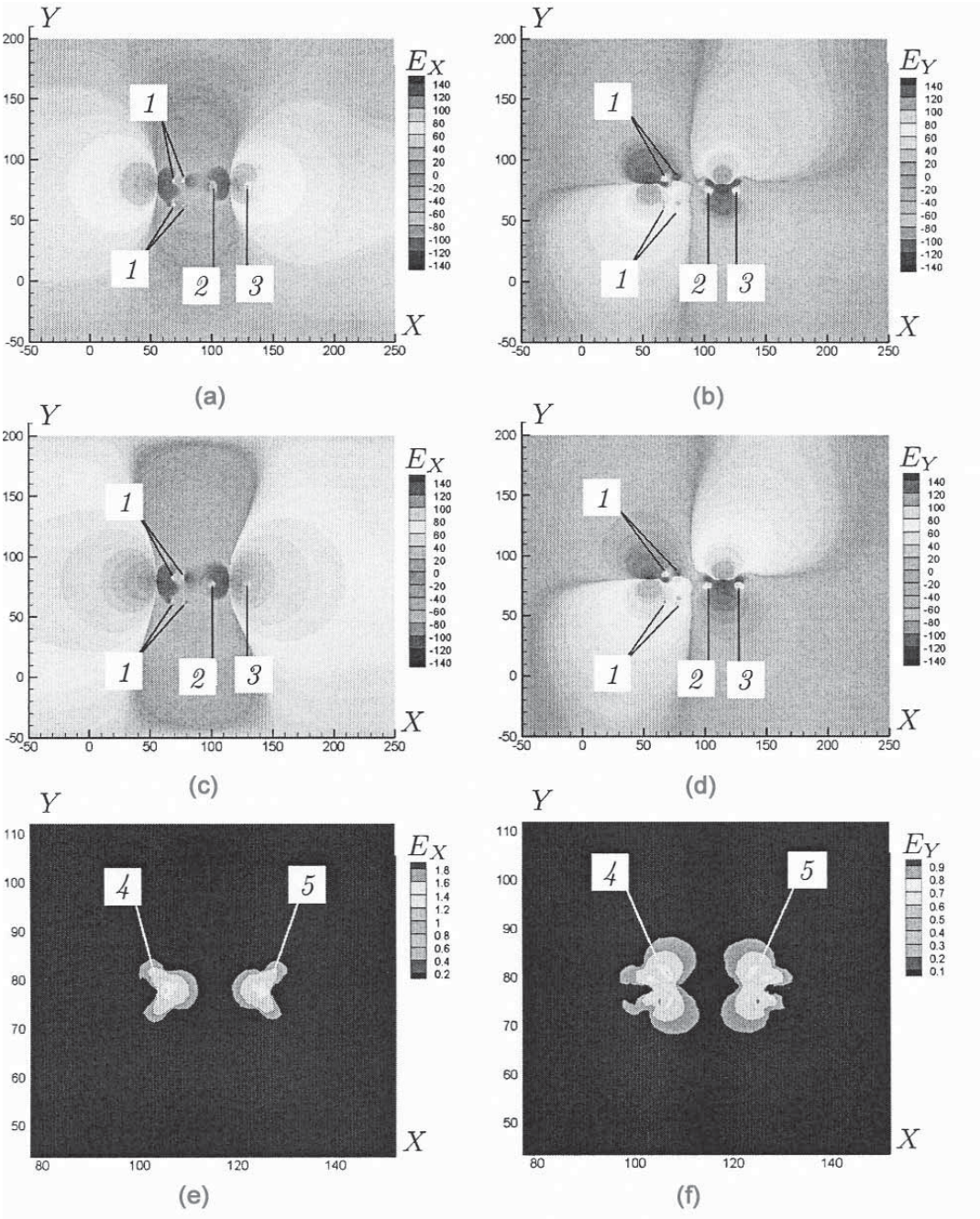

Fig. 4. Distribution of electric field in the XOY section ($Z = 0$): X-component (a) and Y-component (b) with thawing zones; X-component (c) and Y-component (d) without thawing zones; anomalous X-component (e) and Y-component (f) caused by the thawing zones.

for the Wenner and dipole-dipole installations [12–14], making $AB/3$ or half the distance between the dipoles, respectively. The up-to-date median estimates [15] are less optimistic and vary from $0.105AB$ to $0.175AB$ for the Wenner-alpha installation and from $0.125AB$ to $0.19AB$, for the Schlumberger installation. Such estimates, which are not related to the measurement errors, create a false idea of the necessary increase of the propagation distance with increasing spacing. However, the fact is not taken into account that, as distance between the electrodes located at A and B increases, the value of the measured potential difference naturally decreases. For fixed minimum magnitude of the measured signal, the relative measurement error increases, while the propagation distance decreases because some

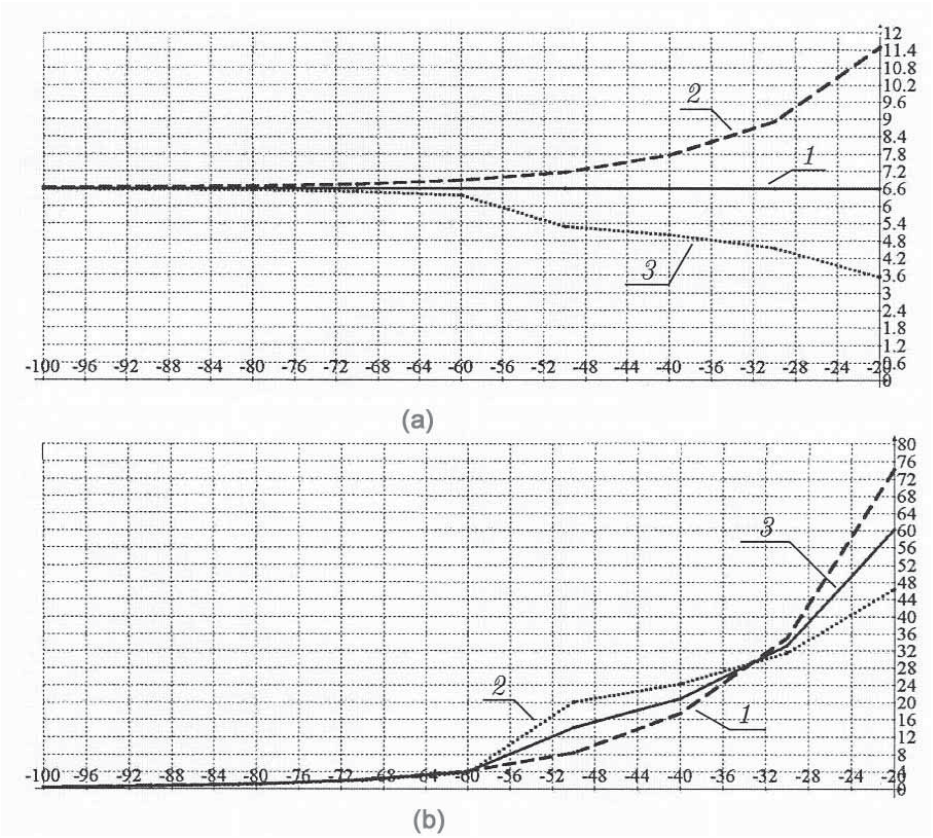

Fig. 5. Dependence of potential difference and relative signal change on the depth of the roof of the test layer (m): (a) difference of potentials (B): here *1* corresponds to half space without the test layer, *2* denotes isolating test layer, and *3* marks conductive test layer; (b) relative change of the signal (%): here *1* corresponds isolating test layer, *2* denotes conductive test layer, and *3* marks the averaged values.

significant part of the signal is due to the noise, not the medium. In the limit case, when the signal becomes less than the minimum measurable, the concept of propagation distance disappears since the measured signals do not contain information about the medium.

Let us estimate the maximum depth at which the Wenner-alpha installation detects a conductive or insulating layer of rather large thickness (as compared with the distance between the electrodes located at the points A and B). Let the spacing be $AB = 60$ m and the installation coefficient factor be $k = 125.6$. Let us put at the depth of 100 m a test layer of thickness of 300 m, isolating (with the electrical conductivity of 10^{-12} Cm/m) or highly conductive (with the electrical conductivity of $769 \cdot 10^4$ Cm/m). We will move it up, approaching the daylight surface in increments of 10 m. Fig. 5 shows the dependence of the measured potential difference at the depth of the roof of the test layer. An object is considered to be detected if the reaction to it is more than twice the measurement error threshold (5 percent) in real conditions.

As is seen from Fig. 5, a noticeable reaction to the object is already observed at the depth from $0.8AB$ to $0.9AB$, which corresponds to the largest estimates of the propagation distance for all possible four-electrode installations [15]. But, it should be taken into account that with such estimation a layer served as a test object was infinite along the strike and the electrical conductivity of it was markedly different from that of the background medium. Therefore, the resulting depth estimate will be considered as the limit rather than the median or medium.

Fig. 6 shows the sections of AR, anomalies and anomalous fields. The following notations are used: *1* denotes the metal supports; *2* marks the left boreholes with the thawing zone, and *3*, the right; *4* corresponds to anomaly, *5* denotes single borehole without thawing zone, and *6* marks the thawing zone.

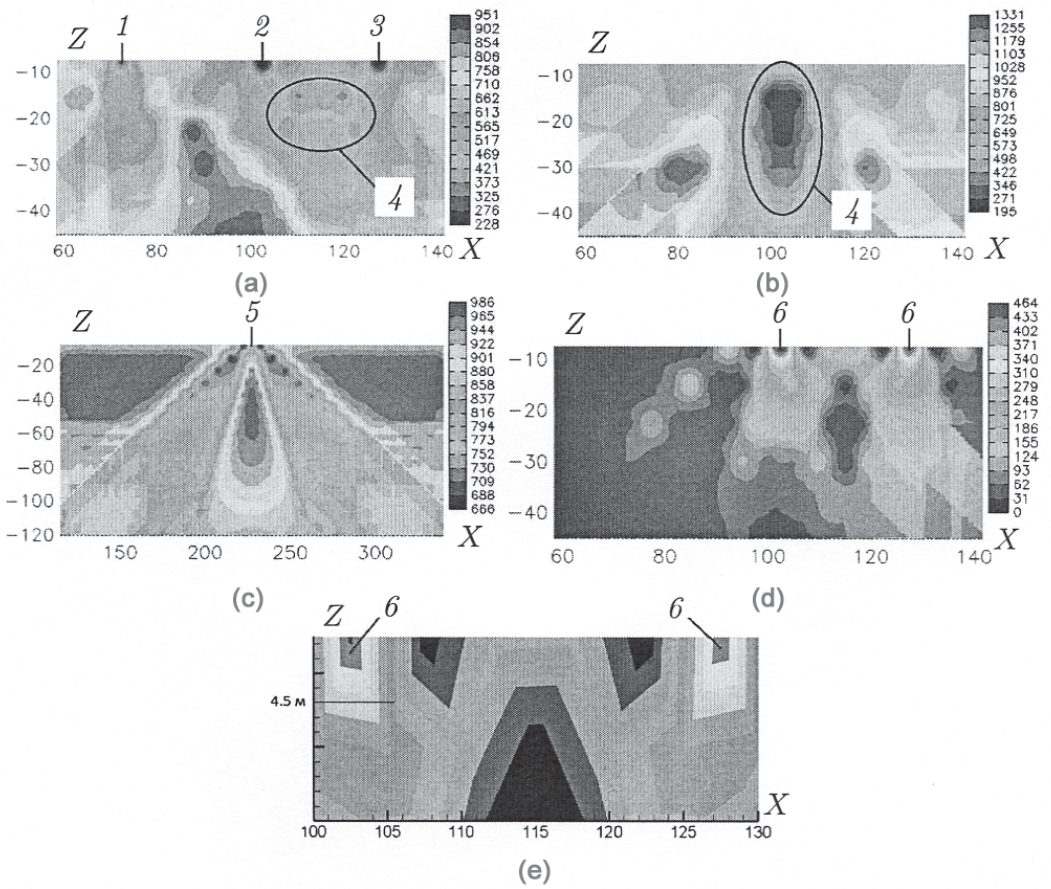

Fig. 6. AR sections, anomalies and anomalous fields: (a) corresponds to AR section (for $Y = 80$ and $Z = 0$) with different position of the installation; (b) shows AR section (for $X = 70$ and $Z = 0$) with different position of the installation; (c) corresponds to AR section (for $Y = 80$ and $Z = 0$) for the single borehole at the center of the domain; (d) shows the distribution of anomalous field (interpolation by using of the Voronoi diagrams); (e) corresponds to the domain with anomalies (interpolation by using the Delaunay triangulation).

In Fig. 6, a, b, and c, the AR distributions are shown to the depth of $AB/2$. Consider the AR on the profile ($Y = 80$ m) across the strike of the largest metal pipe lying on the П-shaped supports (Fig. 1, a). From Fig. 6, a, it is seen that, on the section of the AR, the metal supports merge into some single "object," the thawing zones stand out quite clearly, while the boreholes form an anomaly in the region between them at conditional depths from about 10 to 25 m. At the same time, the effect of the long pipe remains minimal. Consider the AR on the orthogonal profile ($X = 70$ m). It is laid in close proximity to the П-shaped supports and parallel to the pipe lying on them (Fig. 1, a). On this section (Fig. 6, b) we can see a low-resistance anomaly due to П-shaped supports. However, its depth (from 10 to 40 m) is significantly greater than in the previous case, although the П-shaped supports themselves are placed not as deep as the boreholes. This anomaly is characterized by such large sizes for two reasons: (a) four П-shaped supports merge into one; (b) the influence is greatly enhanced of the pipe located on the supports because, on the entire profile, it is above the feeding and measurement electrodes.

Consider a model with a borehole with metal pipe casing located at the center of the domain, where the electro-tomography is performed (Fig. 1, a). All dimensions and electrical parameters are identical to the previous model. The depth of the borehole is increased to 100 m. The number of possible locations of the Wenner-alpha installations on the profile is also increased from 63 to 392 in accordance with the increased borehole depth. The AR section is shown in Fig. 6, c. It is seen that even a single cased borehole generates an anomaly of complex structure. Its central part is occupied by a high-resistance drop-shaped region immersed in the trapezoidal region of average values of AR. In the upper part of

the section near the borehole, there are distinguished slanting strips of low AR values. The presence of a trapezoidal anomaly is due to the fact that the casing metal pipe itself becomes a source of current which flows from its surface into the environment. Such a complex distribution of AR will undoubtedly impede the correct operation of inversion algorithms [16].

On the other hand, if the original task is to detect only individual objects then it is impossible to recourse to complex and inefficient inversion algorithms. For example, conducting numerical simulation of the original problem without thawing zones (Fig. 1, a) and calculating the anomalous field (modulus of the difference of fields) of electrical potential, we can obtain the distribution in which the thawing zones are clearly distinguished (Fig. 6, d). In this case, the values of AR cannot be calculated. But, it is possible to establish the presence of an anomaly and with fairly accurate information about its size both in width and in depth (judging by Fig. 6, e). If there is a presumed model of the medium and objects in it and there are measurements taken in the field then, by calculating the differences of the electric potential fields, we can determine how accurate is the original model and where exactly its estimates are "violated." The difference between long-term observations of this type can inform the researcher about where and how the model changes, which is also important.

CONCLUSION

Experiments on the multiple well platform were conducted which showed that the presence of highly conductive objects both in the considered medium and above it can lead to significant anomalies in the model of apparent resistances. The inversion algorithms can only partially suppress these anomalies. In this case, the preliminary modeling of the direct problem allows us to determine the profile points which can be excluded from the initial model to reduce the influence of highly conductive objects.

In the course of the studies, the software algorithms were implemented that allow us to carry out the calculations for direct problems in the domains of complex shapes, eliminate from the initial model the points unnecessary for the researcher, receive an anomalous field, and perform graphical analysis of the data. All results are obtained directly with the implemented software package and minimal use of some third-party software.

REFERENCES

1. K. S. Sergeev et al., "Studying the Permafrost by Using the Complex of Engineering Geophysics Methods (with a Multiple Well Platform of an Oil-Gas Condensate Field in Western Siberia by Example)," Inzhenern. Izyskaniya No. 10–11, 46–53 (2015).
2. S. A. Akulenko et al., *Electrical Prospecting by the Method of Resistances*: Textbook (Izd. Moskov. Gos. Univ., Moscow, 1994) [in Russian].
3. D. A. Stretton, *Theory of Electromagnetism* (Gostekhizdat, Moscow, 1948) [in Russian].
4. O. Zenkevich, *Method of Finite Elements in Engineering* (Mir, Moscow, 1975) [in Russian].
5. O. Zenkevich and K. Morgan, *Finite Elements and Approximation* (Mir, Moscow, 1986) [in Russian].
6. M. Yu. Balandin and E. P. Shurina, *Methods for Solving SLAEs of Big Dimension* (Novosib. Gos. Tekhn. Univ., Novosibirsk, 2000) [in Russian].
7. I. A. Dobrokhotova and K. V. Novikov, *Electrical Prospecting: Textbook* (Izd. RGGRU, Moscow, 2009) [in Russian].
8. I. E. Blessing, R. N. Funmilola, and P. A. Ahzegbobor, "Estimation of Hydraulic Parameters from Vertical Electrical Resistivity Sounding," J. Inform. Math. Sci. **9** (2), 285–296 (2017).
9. A. V. Skvortsov, *Delaunay Triangulation and Its Application* (Izd. Tomsk. Gos. Univer., Tomsk, 2002) [in Russian].
10. Ph. Preparata and M. Sheimos, *Computational Geometry. Introduction* (Mir, Moscow, 1989) [in Russian].
11. C. Schlumberger and M. Schlumberger, "Depth of Investigation Attainable by Potential Methods of Electrical Exploration," AIME Trans. Geophys. Prospect., pp. 127–133 (1932).
12. R. K. Frohlich, "The Depth Penetration of Dipole Arrays Compared with the Schlumberger Arrangement," Geoexploration No. 5, 195–203 (1967).
13. G. V. Keller, "Dipole Method for Deep Resistivity Studies," Geomorphology. **31** (6), 1088–1104 (1966).
14. A. A. R. Zhody and D. B. Jackson, "Application of Deep Electrical Sounding for Groundwater Exploration in Hawaii," Geophysics **34** (4), 584–600 (1969).
15. S. Szalai, A. Novak, and L. Szarka, "Depth of Investigation and Vertical Resolution of Surface Geoelectric Arrays," J. Environ. Eng. Geophys. **14** (1), 15–23 (2009).
16. C. Rücker, *Advanced Electrical Resistivity Modelling and Inversion Using Unstructured Discretization*, PhD Thesis (Leipzig, 2011).